

Paleoceanography and Paleoclimatology®

RESEARCH ARTICLE

10.1029/2024PA004999

Precession Controls on Climate and Water Isotope Signals in Northern Africa

Xiaoxu Shi^{1,2} , Martin Werner² , Hu Yang¹ , Qinggang Gao^{3,4,5}, Jiping Liu^{1,6} , and Gerrit Lohmann² 

¹Southern Marine Science and Engineering Guangdong Laboratory (Zhuhai), Zhuhai, China, ²Alfred Wegener Institute, Helmholtz Center for Polar and Marine Research, Bremerhaven, Germany, ³Ice Dynamics and Paleoclimate, British Antarctic Survey, Cambridge, UK, ⁴Department of Earth Sciences, University of Cambridge, Cambridge, UK, ⁵Now at School of Geography, Earth and Atmospheric Sciences, The University of Melbourne, Melbourne, VIC, Australia, ⁶School of Atmospheric Sciences, Sun Yat-sen University, Zhuhai, China

Key Points:

- Earlier onset, shorter duration of West Africa summer monsoon occurs at minimum precession, tied to Sahara Heat Low, insolation and interhemispheric contrast
- Properties of Northern Atlantic rainfall sources shift with precession, with broader latitude, higher SST and humidity at minimum precession
- During Green Sahara phases, the isotope variances over Northern Africa mainly reflect changes in upstream (rather than local) rainfall amount

Supporting Information:

Supporting Information may be found in the online version of this article.

Correspondence to:

X. Shi,
shixiaoxu@sml-zhuhai.cn

Citation:

Shi, X., Werner, M., Yang, H., Gao, Q., Liu, J., & Lohmann, G. (2025). Precession controls on climate and water isotope signals in Northern Africa. *Paleoceanography and Paleoclimatology*, 40, e2024PA004999. <https://doi.org/10.1029/2024PA004999>

Received 15 AUG 2024

Accepted 11 JAN 2025

Author Contributions:

Conceptualization: Xiaoxu Shi, Hu Yang

Data curation: Xiaoxu Shi

Formal analysis: Xiaoxu Shi

Methodology: Xiaoxu Shi, Hu Yang, Qinggang Gao

Project administration: Martin Werner

Supervision: Martin Werner

Validation: Xiaoxu Shi

Visualization: Xiaoxu Shi

Writing – original draft: Xiaoxu Shi

Writing – review & editing: Xiaoxu Shi, Martin Werner, Hu Yang, Qinggang Gao, Jiping Liu, Gerrit Lohmann

Abstract Precessional forcing is a key driver of quaternary climate change. Based on 24 experiments covering a full precession cycle, this study explores spatio-temporal variations of both climate and isotope signals in Northern Africa. We find a synchronous phasing of precipitation variations with solar radiation levels and an asynchronous timing of surface air temperature changes across different sub-regions of Northern Africa. Based on daily precipitation, our results reveal earlier onset and withdrawal, as well as a shorter duration of the West Africa summer monsoon (WASM) at minimum precession compared to maximum precession. The onset of the WASM is controlled by the intensity of the Sahara Heat Low, while the monsoon termination is linked to subtropical solar radiation and interhemispheric thermo contrast. Using a novel scale-flux tracing technique, we find that, precipitation during minimum precession is more influenced by evaporation from warmer and more humid regions compared to maximum precession. Additionally, certain inland areas of Northern Africa exhibit positive temporal isotope-precipitation gradients, violating the “amount effect.” This phenomenon mainly occurs during precession phases associated with Green Sahara periods. The isotope composition changes in such places primarily reflect changes in upstream rainfall quantity, rather than changes in local precipitation as is inferred from present day analogs. Conversely, the “amount effect” remains applicable during dry periods in Africa when the Sahara desert is present. This suggests that isotope-based reconstruction of past precipitation variations during Green Sahara periods over Northern Africa needs to be taken with caution.

1. Introduction

As a key component of the global climate system, the climate of Northern Africa, particularly with regard to local precipitation, holds high socio-economic importance (Odoulami & Akinsanola, 2018). The continent features a remarkable diversity of climate regimes. The equatorial (the so-called “tropical wet”) regions experience abundant rainfall throughout the year, sustaining lush rainforests and supporting agricultural activities. The “tropical wet-and-dry” regions (typically within 10–25°N) undergo distinct wet and dry seasons, with the distribution and timing of precipitation varying greatly. The “subtropical Mediterranean” regions, on the other hand, witness wet winters and hot, dry summers. Additionally, the vast desert regions, such as the Sahara, are characterized by extreme aridity, with minimal precipitation and significant temperature fluctuations between day and night. A critical climatic feature of the region is the West Africa summer monsoon, which significantly influences seasonal rainfall patterns in the Sahel and surrounding areas. These diverse climates exhibit varying degrees of temporal variability, spanning from decadal to orbital time scales, shaping the region's complex climatic and hydrological dynamics.

Proxy evidence from Northern Africa and its surrounding oceans reveals significant influences of orbital forcings on the climate of Northern Africa (Larrasoana et al., 2003; Rossignol-Strick, 1985; Van der Laan et al., 2012), primarily driven by the precession cycle that regulates both magnitude and seasonality of incoming solar radiation in the tropical and subtropical regions (Armstrong et al., 2023; Pokras & Mix, 1987). An expression of the obliquity signal and a 400-kyr long eccentricity cycle have been clearly observed as well (Larrasoana et al., 2003; Lourens et al., 2001). Moreover, R. R. Kuechler et al. (2018) identify two modes of astronomical forcings: During eccentricity maxima, the West African monsoon was paced by precession. However, during eccentricity minima, when precession-driven variations in local insolation were modest, changes paced by obliquity became prominent.

Besides proxy-based reconstructions, there are a number of model studies that aim to examine the impact of astronomical factors on the Northern Africa climate. In a 130,000-year transient simulation, leads and lags of monthly climatic variables over Northern Africa are found with respect to precession (Tuenter et al., 2005). Precession also impacts the seasonal timing of maximum precipitation (Tuenter et al., 2003). Marzocchi et al. (2015) investigate the influence of orbital forcing on the Northern Africa climate, by carrying out a set of 22 equilibrium simulations, which covers an entire precession cycle during the late Miocene period. Their results demonstrate that the seasonal distributions of both temperature and precipitation in Northern Africa undergo substantial variations over the course of a full precession cycle. Results from a 140,000-year transient simulation indicate that large precession-forced climate extremes occur in Northern Africa during interglacial time: Higher insolation seasonality happens around precession minimum, accompanied by an increase in vegetation cover and a more intense and northward extended summer monsoon rainfall. In contrast, the opposite phenomena appear during precession maximum (J. E. Kutzbach et al., 2020).

So far, there are very limited model studies that specifically investigate precession effects on Northern Africa climate. Tuenter et al. (2003) isolate the precession/obliquity signal in time-slice experiments using a coupled model of intermediate complexity (ECBilt). They discover that at minimum precession and maximum obliquity, there is an amplified precipitation maximum and a greater northward extension compared to maximum precession and minimum obliquity. Additionally, they also find that the precipitation response to precession is independent of obliquity. Sensitivity experiments based on EC-Earth further reveal that increased moisture transport from both the northern and southern tropical Atlantic is responsible for the precession effects in the Northern African region at minimum precession phases (Bosmans et al., 2015).

The aforementioned model studies mainly concentrate on the precession effects on climatic variables, both on an annual and seasonal time scales. Nevertheless, there is a lack of explorations pertaining to alternative processes such as extreme events, duration of summer monsoon, as well as moisture source locations and properties. Extreme events can not be resolved by proxy records due to their relatively low temporal resolution. But model simulations can provide climatic variables in daily frequency, making them suitable for this type of study. A recent study by Shi et al. (2024) reveal that, in comparison to the present, the last interglacial period experienced an increased Northern Hemisphere summer insolation and a more intensified West Africa summer monsoon. However, despite these changes, the monsoon season was significantly shorter due to an earlier southward shift of the subsolar point during boreal autumn. This implies a potential precessional influence on the duration of monsoon season. In addition, changes in moisture sources can also exert an important impact on the Northern Africa climate, in particular the monsoon system. Precession affects the intensity and seasonality of incoming solar radiation, which in turn influences temperature and atmospheric circulation. Consequently, the main region of moisture source for continental precipitation is anticipated to shift in response to precession. This shift is associated with moisture flux and transport pathway of water vapor, thus affecting the intensity and distribution of precipitation (Gimeno et al., 2020; Jiang et al., 2017). For example, moisture fluxes from the tropical Atlantic are almost in phase with rainfall in West Africa (Gong & Eltahir, 1996). Thus it is anticipated that a decrease in the percentage of moisture sourced from this area would lead to a dryer condition in West Africa. Moreover, the properties of moisture source region also play a role in shaping the monsoon precipitation: the source temperature can impact the amount of water vapor that the atmosphere can hold and transport. In addition, if the moisture source area is more humid than average, the monsoon precipitation tends to be more intense due to a larger amount of water vapor in the air that can be transported to the monsoon region. An innovative water tracing diagnostics has been developed by Gao et al. (2024) in the atmospheric general circulation model ECHAM6. This method offers comprehensive insights into the precise locations and characteristics of moisture sources. Here, we make use of this water tracing diagnostics in our model study.

Stable water isotopes are natural tracers in the water cycle and can serve as valuable indicators of past climate change (Dansgaard, 1964; Fleitmann et al., 2004; Ku & Li, 1998; McManus et al., 1999). It is generally accepted that changes in isotope composition in (sub)tropical speleothems reflect the isotopic composition of local precipitation (X. Liu et al., 2020; Orland et al., 2015). Over subtropical continents, the isotopic signature in speleothems has often been used as an indicator for the intensity of monsoon rainfall (Cheng et al., 2016; Tan et al., 2020). However, this isotopic signal is also sensitive to a number of other variables, including local temperature, specific humidity, and atmospheric circulation (Lachniet, 2009). Therefore, it is possible that the isotopic composition determined from subtropical speleothems does not exclusively represent the local precipitation rate. For example, Pausata et al. (2011) point out that the isotopic records of eastern Chinese caves are

indicators of remote changes in the Indian basin associated with Heinrich events. LeGrande and Schmidt (2009) suggest that millennial isotope changes inferred from tropical interior Asian speleothems are recording alterations in water vapor export out of the tropics, and not local changes in precipitation. Moreover, changes in moisture source (Cheng et al., 2012) or precipitation seasonality (J. Kutzbach et al., 2014) can also affect isotope variations documented in speleothems.

In the present work, we carry out 24 simulations using the AWIESM2 model with enabled water isotope and water tracing diagnostics, with precession values incremented from 0° to 345° with an interval of 15°. To enhance the precession-induced climatic signal, we set eccentricity to a high level, that is, 0.058. Modeled daily precipitation amounts are stored in order to examine extreme events, and onset, withdrawal and duration of the summer monsoon in Northern Africa. Phasing of temperature, precipitation, vegetation, and locations and properties of moisture source are analyzed. Moreover, we examine the isotope changes and isotope-precipitation relationship over the course of a precession cycle.

2. Methods

2.1. Model Description

This study utilizes AWIESM2-wiso, a newly-developed isotope-enabled climate model (Shi et al., 2023). The atmosphere component is ECHAM6-wiso, built upon the general circulation model ECHAM6 (Stevens et al., 2013) but enhanced by stable water isotopes (Cauquoin & Werner, 2021) and water tracing diagnostics (Gao et al., 2024). It contains a land-surface component known as JSBACH, which calculates the boundary conditions (e.g., water, energy, vegetation, and momentum) for the atmosphere model ECHAM6 over terrestrial areas (Raddatz et al., 2007). JSBACH is based on a land surface tiling and contains dynamic vegetation with multiple plant functional types plus two kinds of bare surface (C. H. Reick et al., 2021; Brovkin et al., 2009; C. Reick et al., 2013). Dynamical vegetation changes simulated within the model are determined by the processes related to natural growing and mortality, and disturbance mortality (Brovkin et al., 2009). The landcover parameterization used in JSBACH is described in more details in C. Reick et al. (2013) and evaluated in Brovkin et al. (2013). Stable water isotopes are incorporated as passive tracers within JSBACH (Haese et al., 2013), but potential fractionation during evapotranspiration processes can occur and influence the isotopic signals of soil water. The ice-ocean component of AWIESM2-wiso is FESOM2, utilizing a multi-resolution dynamical core based on finite volume formulation (Danilov et al., 2017). The atmosphere grid applied in the present study is T63L47, which has a global mean spatial resolution of 1.9° with 47 vertical levels. For the ocean, a spatially varied resolution is used (Figure S1 in Supporting Information S1), from about 100 km in the open ocean to 25 km over polar areas and 35 km for the equatorial belt and along coastlines. There are 46 uneven vertical layers in the ocean.

2.2. Experimental Design

We first perform a pre-industrial (PI) equilibrium simulation, initialized from the Atmospheric Model Inter-comparison Project (AMIP) (Roeckner et al., 2004) and the World Ocean Atlas (WOA) climatological temperature and salinity data for the years 1950–2000 (Levitus et al., 2010). We run the PI simulation for 1,500 model years with dynamic vegetation and water isotopes. The boundary conditions for PI are configured in accordance with the criteria of PMIP4 (Otto-Bliesner et al., 2017). Branched off from the PI run, we conduct 24 equally precession-spaced experiments. The 24 simulations only differ in their prescribed precession which ranges from 0° to 345° with an interval of 15°. Thus, each simulation represents a specific phase of a precession cycle. To enlarge the precessional influence, the eccentricity is adjusted to 0.058, a possible maximum value in the past one million years. The obliquity is set to be 24.5°. Other boundary conditions, including greenhouse gases, topography, and ice sheets, remain unchanged. These experiments are labeled P_i , where i corresponds to the value of precession. All of the 24 equally precession-spaced simulations are integrated for 300 model years with water isotope diagnostics, and we consider the first 200 model years as spin-up. Since simulations with water tracing diagnostics are computationally very expensive, we switch on the water tracing diagnostics for only the final 30 model years, so that the locations and properties of moisture source can be traced during the model integration.

2.3. Calendar Adjustment

Seasonal changes of the climate are predominantly shaped by fluctuations in precession and eccentricity. In paleoclimate research, application of the present-day calendar can introduce artificial bias regarding the calculated seasonality of climatic variables, as the lengths of the months and seasons change across the precession cycle (Bartlein & Shafer, 2019; Berger et al., 2024; Jousaume & Braconnot, 1997; Shi et al., 2022). Unlike the present-day calendar, in which the lengths of the months and seasons are fixed, the celestial calendar determines the lengths of months and seasons according to astronomical positions. It thus aligns well with the fluctuations in solar radiation throughout the course of the year. For each experiment, we convert the present-day calendar, which serves as the standard configuration in the model, into the celestial calendar using the methodology outlined in Shi et al. (2022). In our study, all results regarding the seasonal means are calculated based on the astronomical seasons for the celestial calendar and we keep vernal equinox fixed at the 21st of March.

2.4. Tagging of Moisture Sources

An innovative scaled-flux tracing method, following the principles introduced in Fiorella et al. (2021), has been implemented by Gao et al. (2024) into the atmosphere component of AWIESM2-wiso. The water tracers are constructed upon the model code framework of water isotopes. The scaled-flux tracing approach exclusively traces the evaporation of moisture from the open ocean. It is used for tagging any characteristic related to evaporation, such as the location (i.e., latitude and longitude), sea surface temperature, wind speed, and humidity. Moreover, this scaled-flux tracing technique also enables the quantification of the amount of moisture derived from land or ocean. For a more complete description of the scaled-flux tracing technique, we refer to Gao et al. (2024).

2.5. Definitions of the Onset/Withdrawal/Duration of West Africa Summer Monsoon

We calculate the onset of West Africa summer monsoon (WASM) based on a widely-employed traditional approach with the use of daily precipitation (Pausata et al., 2016; Sultan & Janicot, 2003). As WASM onset is marked by an abrupt latitudinal shift of the Intertropical Convergence Zone (ITCZ) from a quasi-stationary south location to a quasi-stationary north location (Sultan & Janicot, 2003), the changes in precipitation at the ITCZ north location can make inference about the arrival of monsoon. As a first step, we perform an Empirical Orthogonal Function (EOF) analysis for each experiment on the continental daily precipitation over the region between 0–40°N and 15°W–20°E over the time period from 1st March to 30th November. This step aims to derive the latitude of the ITCZ during monsoon (north location) and pre-monsoon phases (south location), which is represented by the first and second EOF maxima respectively. Next, we compute for each experiment the zonally averaged precipitation over 15°W–20°E at its respective north location of ITCZ from 1 June to 31 July. The obtained time series is filtered using a running mean analysis to remove variability with a period shorter than 10 days. The monsoon's onset is determined as the day preceding the largest increase in the filtered precipitation, and the withdrawal is defined as the day when the filtered precipitation drops below 2 mm/day for a continuous period of at least 20 consecutive days. The duration of WASM is simply the time interval between its onset and withdrawal.

2.6. Isotope-Precipitation Relationship

Similarly to previous research (Cauquoin et al., 2019; Risi et al., 2010; Roche & Caley, 2013; Schmidt et al., 2007), we compute for each grid box the interannual correlation coefficients and gradients between monthly anomalies of oxygen-18 composition in precipitation ($\delta^{18}O_p$) and precipitation rate. This analysis is conducted over a 100-year period in each of the 24 simulations. To remove the seasonal cycle, we subtract the multi-year mean value of each month from the corresponding monthly mean value. Only the grid boxes having a mean precipitation larger than 250 mm/year are considered in our analysis (Cauquoin et al., 2019). By implementing such a threshold, we eliminate grid cells with excessively low precipitation rates.

Moreover, we calculate the temporal $\delta^{18}O_p$ -precipitation slope between two experiments as:

$$m = (\delta^{18}O_{p,EXP1} - \delta^{18}O_{p,EXP2}) / (P_{EXP1} - P_{EXP2}) \quad (1)$$

P represents annual mean precipitation, whereas EXP1 and EXP2 refer to two specific experiments of the 24 precession sensitivity simulations. In order to perform such an analysis through a complete precession cycle, for each experiment P_i (where $i = 000, 015, 030 \dots 345$), we calculate its temporal $\delta^{18}\text{O}_p$ -P slope in relation to P_{i+45} . Here a precession distance of 45° is chosen in order to ensure a substantial precipitation differences between the two experiments involved here. We only consider the grid boxes with an annual mean precipitation being larger than 250 mm/year in both P_{i+45} and P_i , thus extreme dry areas with very low rainfall rate are excluded from our calculation. Moreover, for numerical reasons, grid boxes with a precipitation anomaly less than 0.5 mm/day between P_{i+45} and P_i are also eliminated. This threshold can help to ensure a dominant precipitation dependence on the isotope signal.

3. Results

3.1. Spatio-Temporal Phasing of Precipitation and Temperature

The spatio-temporal phasing of Northern African precipitation during JJAS in a full precession cycle is illustrated in Figure 1. There is a close association between the precipitation and the amount of solar radiation received between 0 and 25°N during boreal summer, with both peaking in P120 and reaching their lowest levels in P300 (Figure 1y). The difference in insolation between P120 and P300 is substantial, amounting to 95 W/m^2 , resulting in a notable difference (more than 5 mm/day) in precipitation amounts across Northern Africa. We also observe a latitudinal distribution of precipitation, with its maxima (exceeding 12 mm/day) occurring at 14°N in P120. As precession progresses toward 300° , this maxima gradually shifts southward to $6\text{--}7^\circ\text{N}$, and decreases to 4 mm/day and lower. In P120, the area experiencing precipitation exceeding 1 mm/day extends considerably north into the Sahara region. However, as the precession advances from 120° to 300° , this area contracts and does not extend beyond 15°N in P300.

Our analysis reveals that both maximum and minimum insolation over most parts of Northern Africa happen at precession Phase 90° , indicating the largest seasonality in P090 (Figures 2a and 2b). The timing of maximum surface air temperature (SAT_{max}) exhibits substantial spatial heterogeneity (Figure 2c) which do not necessarily correspond to the spatio-temporal phasing of maximum solar insolation. We can divide Northern Africa into three main regions: the northern dry region (north of 26°N), the central transitional region ($8^\circ\text{N}\text{--}26^\circ\text{N}$), and the southern humid area ($0\text{--}8^\circ\text{N}$). The northern dry region experiences minimal rainfall (Figure 1) and cloud cover (Figure S2 in Supporting Information S1) throughout the full precession cycle, leading to direct regulation of SAT_{max} by the phasing of maximum insolation, which peaks at P090. In contrast, the southern humid area, where deep convection occurs during the warm seasons in all precession phases, exhibits maximum cloud cover when convection is at its peak, resulting in SAT_{max} being associated with minimum precipitation, typically around P300. Timing of SAT_{max} in the central transitional region exhibits a latitudinal heterogeneity, which is predominantly influenced by the combined impact of solar insolation magnitude and deep convection intensity. In contrast, the timing of minimum surface air temperature (SAT_{min}) shows a more spatially synchronized phasing, occurring at around 90° precession across most areas of Northern Africa (Figure 2d), closely following the timing of minimum insolation (Figure 2b). This synchronized phasing of SAT_{min} results from minimal cloud cover in winter, allowing surface temperatures to respond directly to solar radiation. In contrast, SAT_{max} occurs under summer monsoon influence, introducing additional factors (e.g., cloud cover, extent of monsoon area) beyond solar radiation.

3.2. Extreme Precipitation Event

Consecutive dry days (CDD) and consecutive wet days (CWD) serve as reliable climate indicators for precipitation extremes, defined as the maximum number of consecutive days with daily precipitation amounts below and above 1 mm, respectively. CDD and CWD are closely associated with the occurrence of droughts and floods. We first look at CDD and CWD in Northern Africa at two precession extremes: precession minimum (P090) and precession maximum (P270).

During P270 in Northern Africa, consecutive rainfall events predominantly occur in tropical regions (Figure 3e). In contrast, during P090, a northward expansion of humid conditions is observed, leading to an overall increase in CWD, particularly south of the Sahel region (Figure 3d). At precession maximum (P270), extreme dryness prevails for most of the year, with CDD ranging between 200 and 365 days in most Sahara regions (Figure 3b).

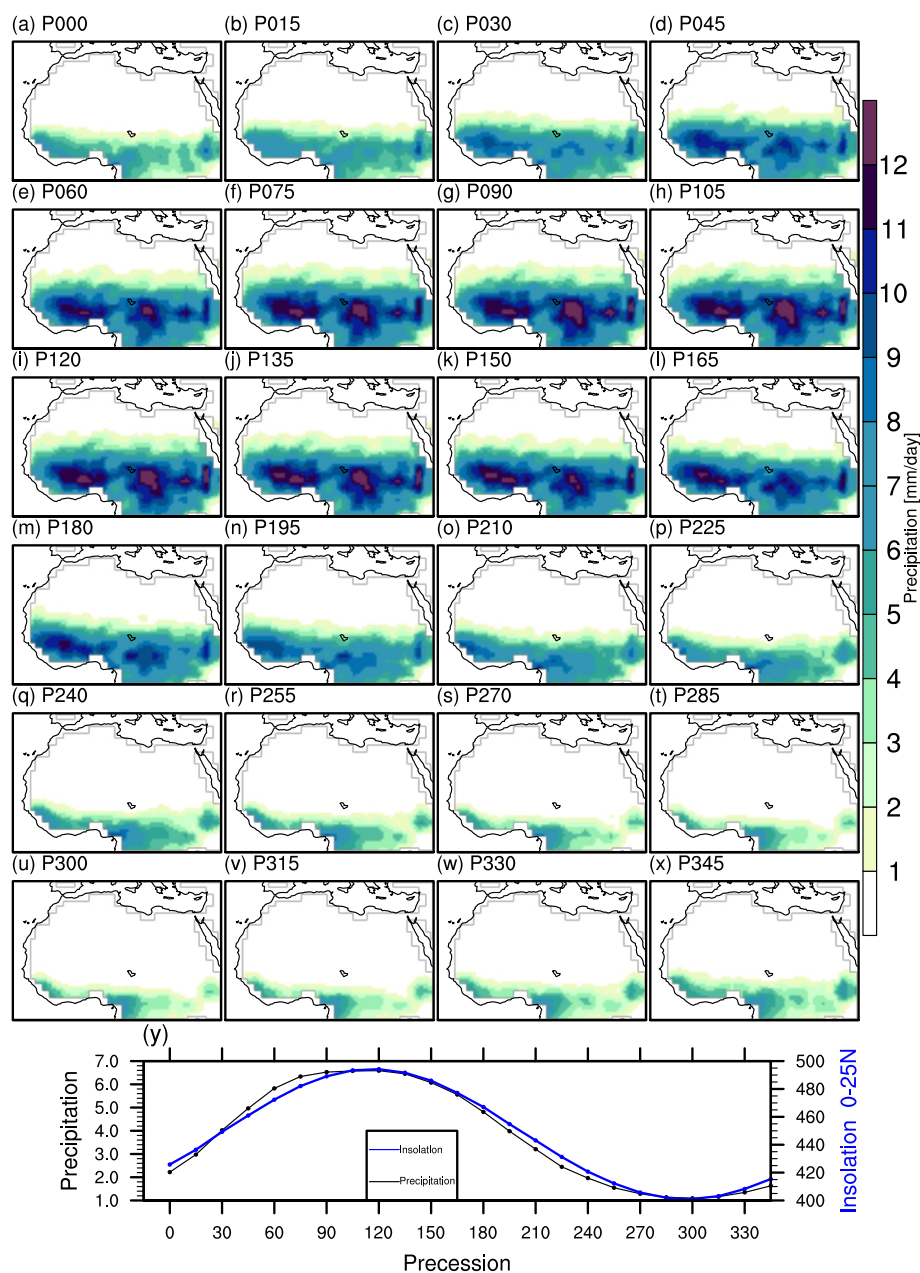


Figure 1. (a–x) Modeled precipitation amount (mm/day) over Northern Africa during JJAS in a full precession cycle. (y) Precipitation (mm/day) over the Northern African continents (0–25°N, 15°W–40°E) during JJAS and 0–25°N solar insolation (W/m^2) during JJA.

Conversely, tropical Africa experiences relatively fewer extreme dry days, with CDD being less than 100 days. This highlights a significant meridional contrast in CDD between the Sahara and lower latitudes during precession maximum. Similar contrasts are observed during precession minimum (P090), albeit less pronounced. In relative to P270, the Sahara experiences less extreme dryness in P090 (Figure 3c), with CDD ranging from 100 to 240 days (Figure 3a). This decrease in CDD is directly linked to enhanced hydrological cycle which leads to increased rainfall amounts over the Sahara region and a northward expansion of humid area.

In a wetter climate, the number of CDD typically decreases, while the number of CWD increases due to more frequent and sustained rainfall. This expected inverse relationship between CDD and CWD is evident in Northern Africa. However, in tropical Africa, despite the generally more humid conditions and an increase in CWD, P090

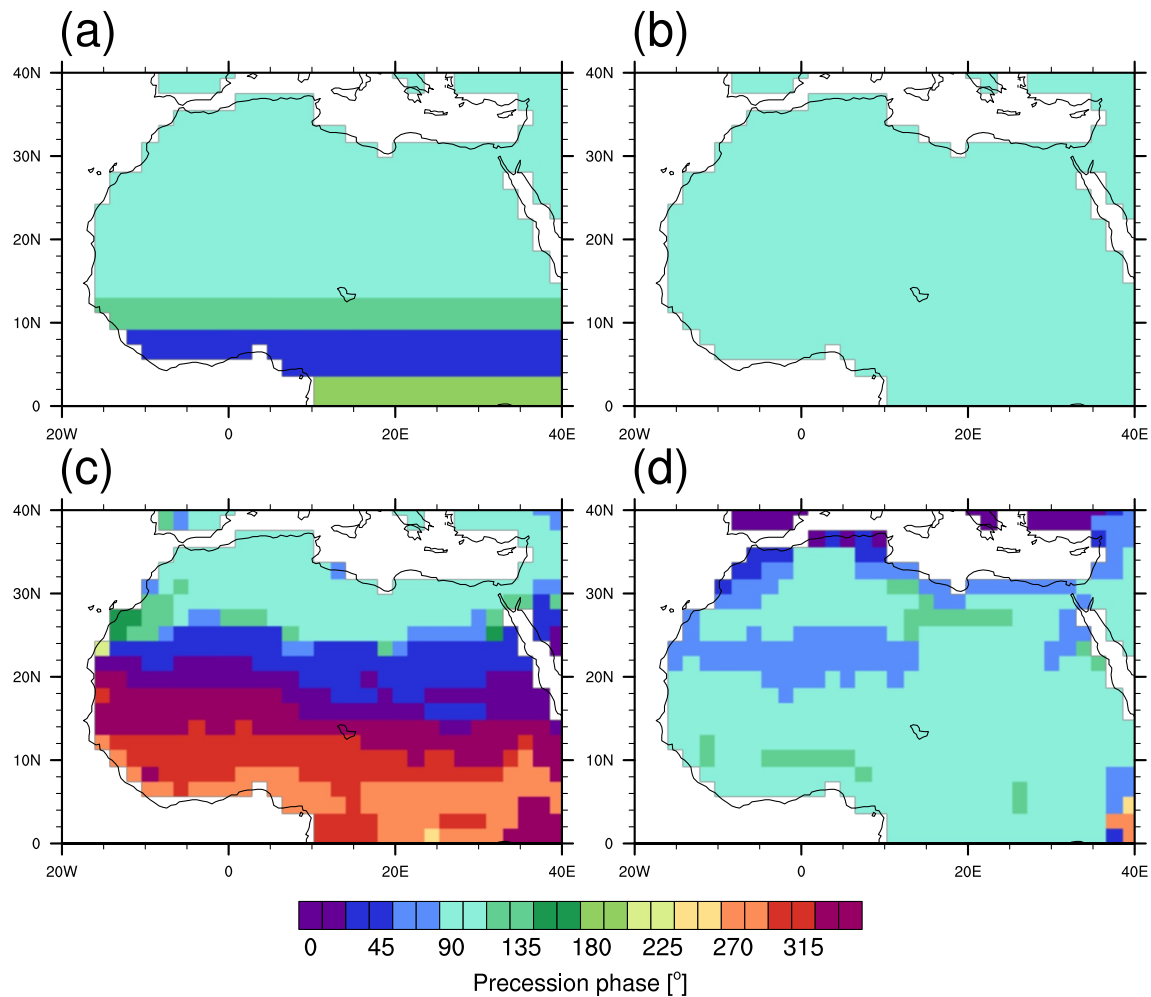


Figure 2. Precession phase ($^{\circ}$) at which the (a) warm-month maximum incoming insolation, (b) cold-month minimum incoming insolation, (c) warm-month maximum surface air temperature, and (d) cold-month minimum surface air temperature occurs.

exhibits a higher frequency of extreme dry events compared to P270 (Figure 3c). This results in a dipole pattern of CDD changes. This phenomenon can be attributed to the earlier southward shift of the solar zenith point from the Northern to the Southern Hemisphere during boreal fall at minimum precession, which shortens the monsoon season and extends the dry period. A more detailed explanation is provided in Section 3.2.

3.3. Length of West Africa Summer Monsoon

The West Africa summer monsoon (WASM) is a phenomenon that occurs on a regional scale and is closely connected to the latitudinal shifts of the ITCZ. In this section, our objective is to determine the onset, withdrawal, and duration of the summer monsoon based on daily precipitation at the north location of the ITCZ (for more information on calculation of the ITCZ location and the WASM onset/withdrawal, please refer to Section 2.5).

Throughout a precession cycle, the onset of the WASM varies between early June and mid-July (Figure 4a). Specifically, the onset tends to happen earlier during the precession phases ranging from 0° to 105° , whereas it is delayed during the phases from 180° to 300° . This timing reversely aligns with insolation during May (Figure 4b). Moreover, our analysis elucidates a notable association between the intensity of the Sahara Heat Low (SHL) in June and the onset of the summer monsoon. Specifically, the SHL (expressed as lower atmospheric thickness in Figure 4c) demonstrates a higher degree of intensity during precession phases ranging from 0° to 120° , while it displays a weakened state during phases from 195° to 315° . Our results align concordantly with previous research,

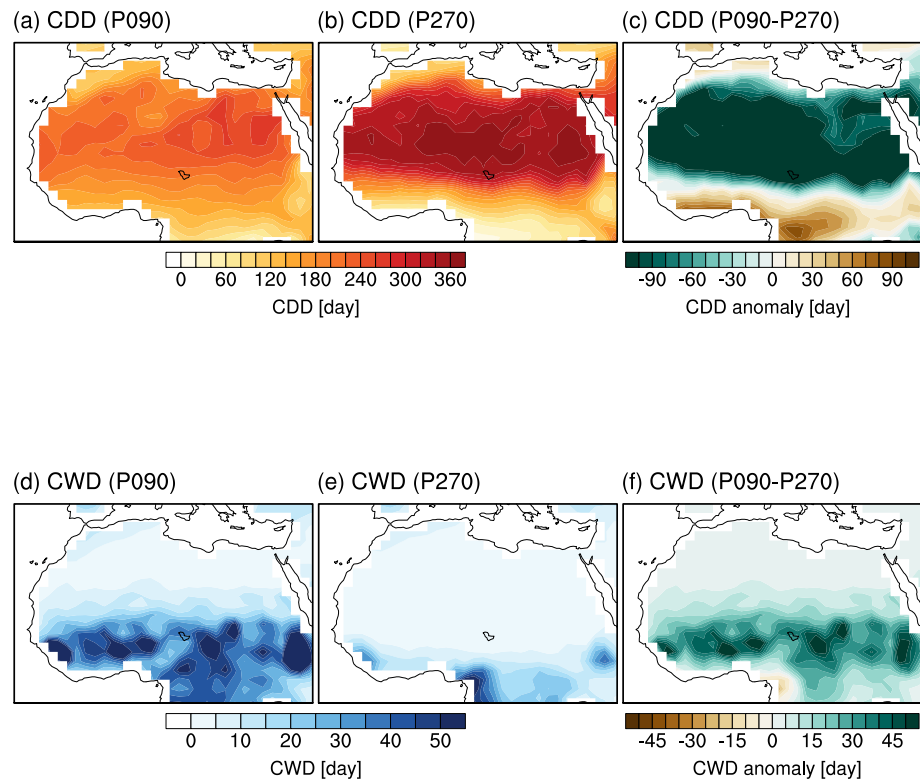


Figure 3. Consecutive dry days (CDD, unit: day) for (a) P090, (b) P270, and (c) P090 minus P270. Consecutive wet days (CWD, unit: day) for (d) P090, (e) P270, and (f) P090 minus P270.

which has posited an amplification of the SHL preceding the arrival of the summer monsoon in late June (Sultan & Janicot, 2003).

The retreat of the WASM, as seen in Figure 4d, generally shows a delaying tendency as precession progresses from 0° to 270° , and an advancing tendency for 270° – 360° . The phasing of the monsoon retreat are governed by two primary factors: (a) the insolation magnitude during August–September (Figure 4e), and (b) the latitudinal displacement of the maximum insolation, denoted as the solar zenith point (Figure 4f). Increased amounts of solar radiation play a crucial role in sustaining the energy necessary for the summer monsoon, hence causing the monsoon to persist longer as the precession shifts from 0° to 180° . Nevertheless, as the precession shifts from 180° to 270° , despite a rise in insolation, there is an earlier migration in the sunlit point toward the Southern Hemisphere. This results in an earlier reversal of the interhemispheric thermal contrast (Figure 4g), thereby prompting the withdrawal of the summer monsoon. Notably, from 270° to 360° , the advancing tendency in the monsoon withdrawal is driven by both a reduction in insolation and an earlier southward shift of the sunlit point. Finally, the duration of summer monsoon is largely shaped by the timing of withdrawal in a precession cycle (Figure 4h).

3.4. Vegetation

Vegetation is a crucial component of the climate system, not only influenced by climatic conditions but also exerting significant feedback on the climate, for example, by regulating surface albedo and surface temperature, and modulating the hydrological cycle through evapotranspiration. Vegetation patterns are inherently linked to precipitation rate, seasonality and duration which are directly influenced by precession. The equatorial region of Africa receives abundant rainfall for most of the year, facilitating the growth of lush forests (Figure 5). Around maximum precession (P270), the formation of forests in this region is predominantly concentrated within a narrow latitudinal range near the equator, particularly in the western equatorial area. As precession progresses from 270° to 90° , the forested area expands northwards due to increased precipitation, reaching as far as 18°N at minimum precession (P090) (Figure 5g).

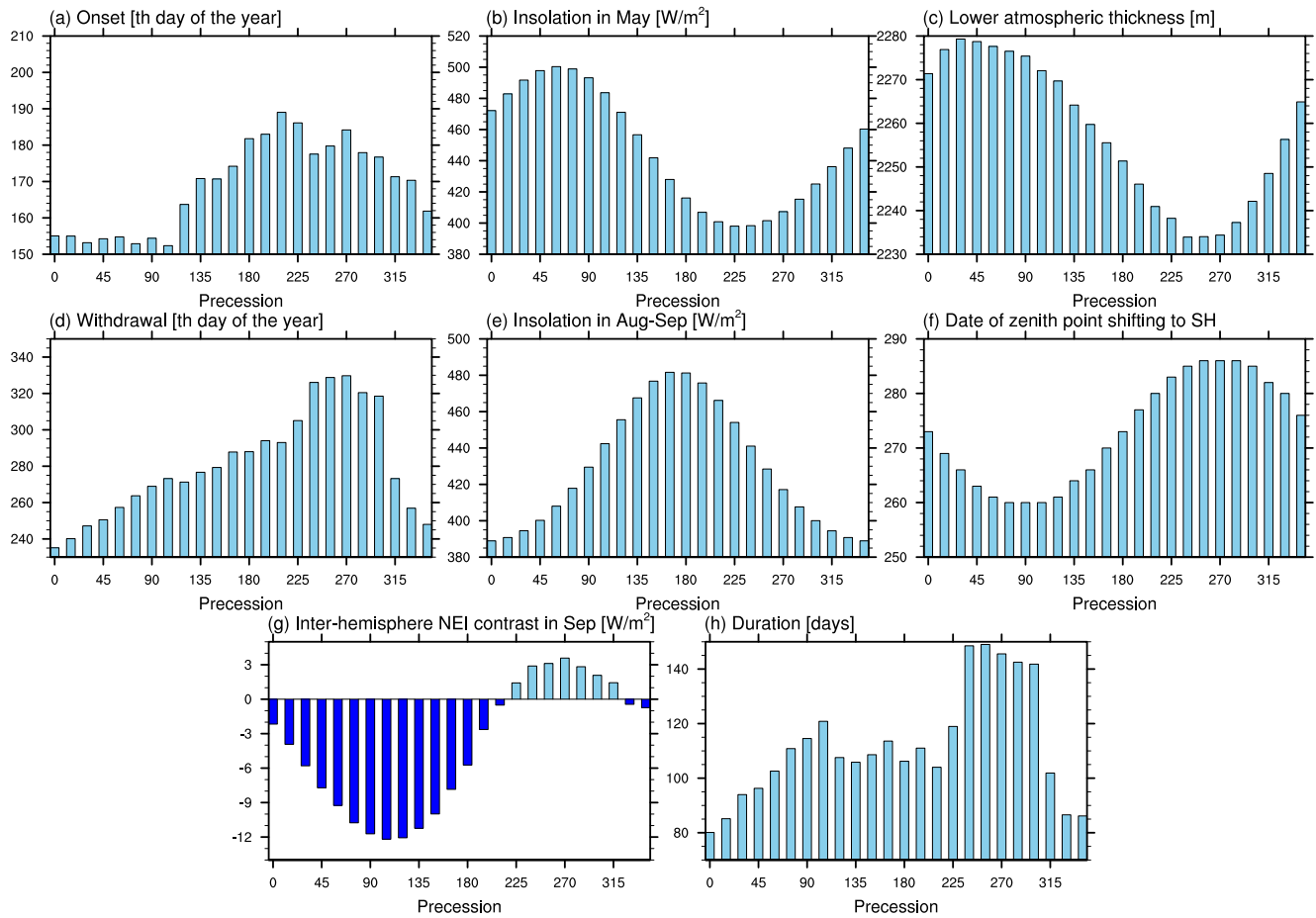


Figure 4. (a) Day of West Africa summer monsoon onset, (b) averaged insolation over 0–25°N during May, (c) lower atmospheric thickness, defined as the anomaly in geopotential height between 750 hPa and 925 hPa over 15–35°N, 20°W–5°E, (d) day of withdrawal of Africa monsoon, (e) averaged insolation over 0–25°N during August–September, (f) day of solar zenith point shifting to Southern Hemisphere, (g) inter-hemisphere contrast in net energy input in September, defined as the anomaly of averaged net energy input between Northern and Southern Hemisphere (negative values in dark blue), and (h) duration of Africa summer monsoon in a precession cycle.

During precession phases ranging from 225° to 345°, the Sahara desert persists (Figures 5r–5x), mainly driven by minimal rainfall (Figure 1) and a high number of consecutive dry days (Figure S3a in Supporting Information S1). The transitional zone between the Sahara desert and the tropical forest undergoes distinct wet and dry seasons during the year, providing suitable conditions for the growth of shrubs and grasses. This transitional zone extends to the northernmost part of Africa during precession phases between 30° and 165° (Figures 5c–5l), while the desert coverage is small.

3.5. Moisture Sources

In our study, we utilize a novel scale-flux tracing method, as described in Section 2.4 and Gao et al. (2024), to track the locations and characteristics of moisture source regions. In the following we focus on the moisture source properties at two precession extremes. For a complete spatial-temporal timing, we refer to Figures S4–S8 in Supporting Information S1.

The mass-weighted mean open ocean evaporative source latitude (hereafter denoted as source latitude) of annual mean precipitation in Northern Africa varies between 8°S and 20°N at minimum precession, and exhibits a latitudinal spread (Figure 6a). Specifically, in Northern Africa, the latitude from which regional rainfall originates tends to be more poleward as the region moves further north or west. During maximum precession, when the humid area is confined to 0–15°N, the source latitude is more restricted, specifically ranging from 4°S to 15°N (Figure 6b). In tropical regions, moisture comes from lower latitudes during the minimum precession phase

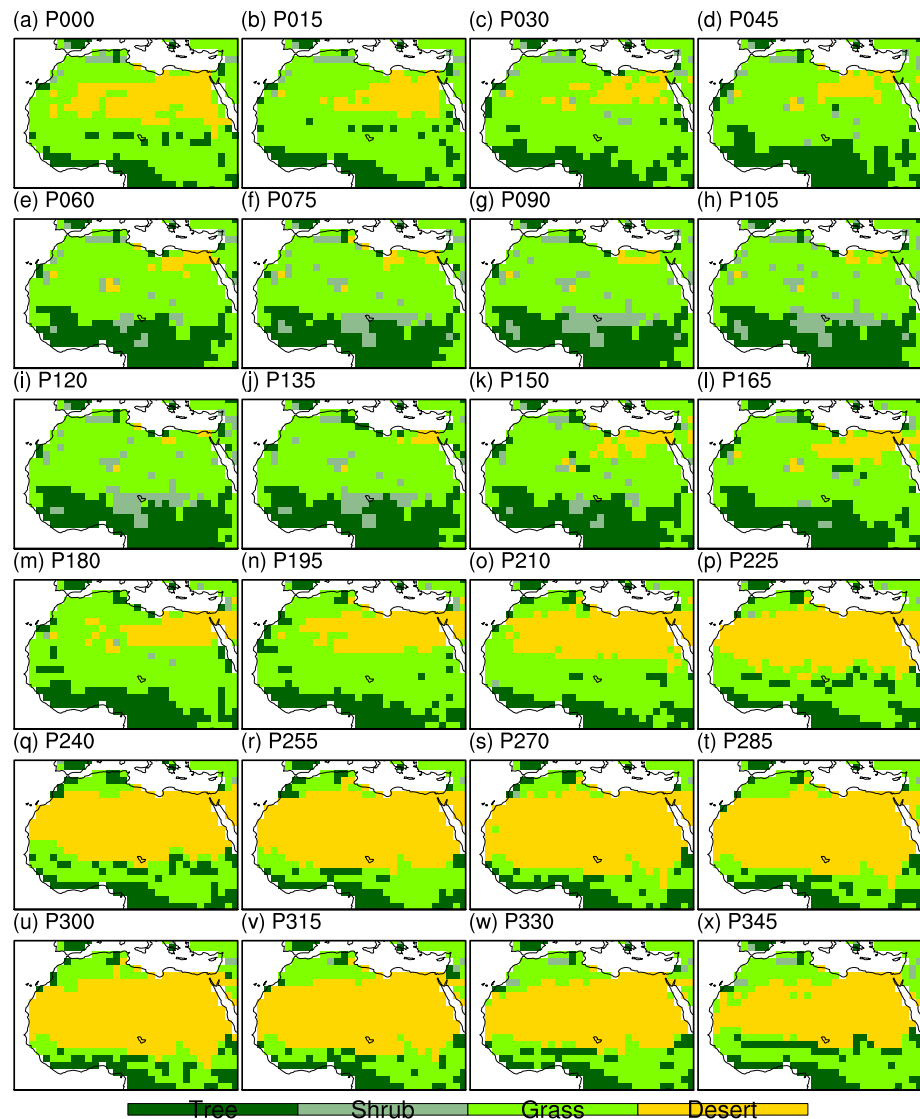


Figure 5. Distribution of main vegetation types across Northern Africa in a precession cycle.

relative to the maximum precession period (Figure 6c). The mass-weighted source longitude, as illustrated in Figures 6d and 6e, also exhibits a prevailing northwest-southeast gradient. In the West African region, moisture is predominantly transported from the adjacent Atlantic Ocean, whereas in tropical eastern Africa, a significant portion of precipitation is sourced from the Indian Ocean. The source longitude for the region between western and eastern Africa spans from 5°W to 30°E, indicative of a blend of moisture contributions from both the Atlantic and Indian Oceans. The P090-minus-P270 source longitude is overall negative (Figure 6f), reflecting that precipitation in Northern Africa at maximum precession is more supplied by moisture originating from the Indian Ocean.

Having examined the moisture source locations, we are now exploring three additional oceanic properties that influence evaporation: sea surface temperature (SST), 10 m wind velocity (wind10), and surface relative humidity (rh2m). The source SST associated with the annual mean precipitation over Northern Africa falls within the range of 24.4–26.5°C in P090 and 23.5–26.5°C in P270 (Figures 6g and 6h). In P090, the area exhibiting the highest source SST is tropical western Africa, where moisture is directly sourced from the Gulf of Guinea characterized by comparatively warmer surface waters. In comparison to P090, for the majority of tropical Africa, precipitation in P270 originates from cooler oceanic regions (Figure 6i), reflecting differences in the source moisture locations (Figures 6c–6f) and the underlying SST distribution (Figure S9 in Supporting Information S1). A noticeable

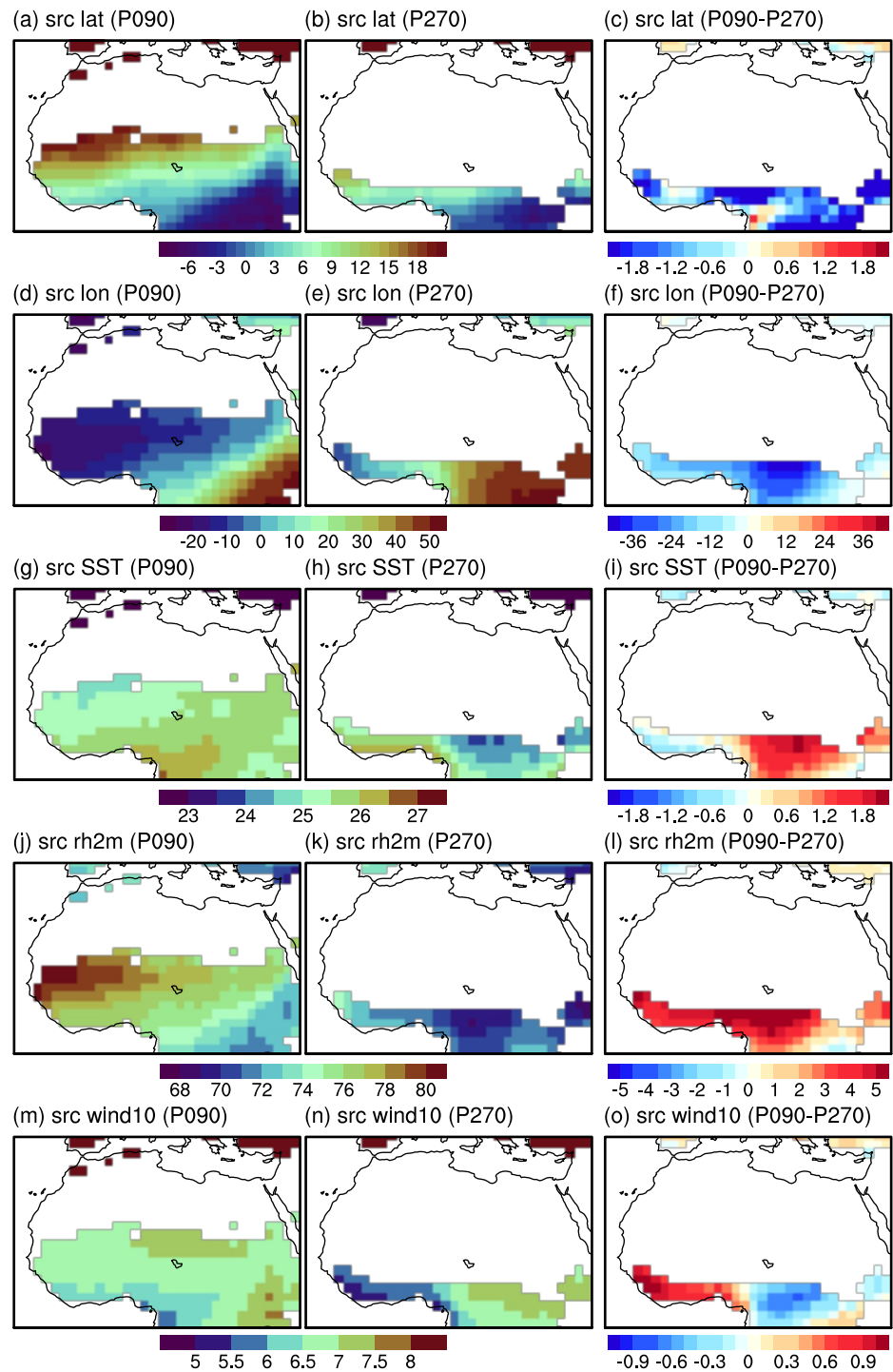


Figure 6. The mass-weighted mean open ocean evaporative source locations and properties for (a–c) latitude [°], (d–f) longitude [°], (g–i) sea surface temperature [°C], (j–l) surface relative humidity [%], and (m–o) 10 m wind speed [m/s]. (a, d, g, j, m) are for P090, (b, e, h, k, n) for P270, and (c, f, i, l, o) show anomaly values for P090 minus P270. Negative latitude (longitude) values refer to the southern (western) hemisphere.

northwest-southeast gradient is evident in the source rh2m associated with the annual mean precipitation in P090, ranging from 71% in tropical eastern Africa to 80% in subtropical western Africa (Figure 6j). Interestingly, such spatial distribution is not seen during the maximum precession phase, with the source rh2m exhibiting more uniform pattern ranging from 69% to 71% across most regions (Figure 6k). In comparison to P090, Northern

Africa derives moisture from sea surface areas characterized by relatively lower relative humidity in P270 (Figure 6l). In both extreme precession phases, source wind10 of annual mean precipitation is relatively smaller (larger) for the tropical western (eastern) Africa (Figures 6m and 6n). This gradient is more pronounced during maximum precession than during minimum precession (Figure 6o).

Moreover, the scale-flux tracing method applied in our model can also tell the percentage of moisture coming from oceans and continents. As seen from Figure S10 in Supporting Information S1, oceanic evaporation is the primary source of precipitation in tropical and subtropical western Northern Africa, as well as in coastal parts of the Indian Ocean. However, it is important to note that a non-ignorable percentage of moisture originates from land, particularly in inland regions where the contribution of continental evaporation to precipitation can exceed 50% (Figure S10 in Supporting Information S1). Changes of continental evaporation source regions and properties are not included in the scale-flux tracing method of ECHAM6-wiso, yet (Gao et al., 2024).

3.6. Isotope

The synchronization of climatic factors such as surface temperature and precipitation in both space and time leaves considerable imprints on the oxygen-18 composition of precipitation (henceforth denoted by $\delta^{18}\text{O}_p$) across Northern Africa (Figure 7). Particularly, the Sudan region exhibits the lowest $\delta^{18}\text{O}_p$ values, whereas higher values are found in the western Africa, forming a distinct zonal gradient. During humid periods in Africa, precipitation is isotopically depleted, and this change can be attributed to increased precipitation amounts. As climate shifts from humid to dry conditions, there is a general enrichment in $\delta^{18}\text{O}_p$ observed across Northern Africa driven by a reduction in the amount of rainfall.

We simulate negative interannual gradients between monthly-mean $\delta^{18}\text{O}_p$ and precipitation rate across Northern Africa in any phase of a precession cycle (Figure 8 and Figure S11 in Supporting Information S1). These gradients typically range from $-0.2\text{‰mm}^{-1}\text{d}$ to $-0.8\text{‰mm}^{-1}\text{d}$, aligning well with previous model studies (Cauquoin et al., 2019; Risi et al., 2010; Schmidt et al., 2007). This phenomenon is known as the “amount effect” (Dansgaard, 1964), and is commonly observed in tropical and subtropical regions.

The interpretation of isotopic records for reconstructing past precipitation variations often relies on the assumption that the modern $\delta^{18}\text{O}_p$ -precipitation relationship serves as an adequate surrogate for the temporal slope of past periods (e.g., Johnson et al., 2006; Maher, 2008). Therefore, it is crucial to assess the validity of this relationship across different phases of the precession cycle. Here, we calculate the temporal $\delta^{18}\text{O}_p$ -precipitation gradients as outlined in Section 2.6, to determine when and where this observed relationship holds true throughout the precession cycle. Figure 9a depicts temporal $\delta^{18}\text{O}_p$ -versus-precipitation gradients across Northern Africa between P_i and P_{i+45} , indicating negative temporal $\delta^{18}\text{O}_p$ -precipitation slopes across tropical and subtropical Africa during the African dry period when the Sahara desert was present, in agreement with the “amount effect.” However, during precession phases 75° – 135° (Figures 9c–9j) characterized by a green Sahara, there is a distinct occurrence of positive temporal $\delta^{18}\text{O}_p$ -precipitation slopes in specific areas of Northern Africa, deviating from the expected “amount effect.”

According to principles already established (Dansgaard, 1964), the isotopic composition of precipitation from a particular air mass is primarily controlled by the fraction of vapor remaining. More rainout from a given air mass leads to a decrease in the delta value of the vapor remaining and the subsequent precipitation. Therefore, apart from the “amount effect,” the $\delta^{18}\text{O}_p$ -signal in Northern African precipitation may be influenced by non-local processes that include: (a) changes in the moisture source region, (b) changes in the moisture source properties, such as SST, surface winds or humidity levels, that impact fractionation of oxygen isotopes at the origin, and (c) changes in the fractionation of oxygen isotopes in the water vapor during transportation to specific location where the vapor is precipitated. Our analysis reveals relatively obvious changes in the geographical locations (Figures S12 and S13 in Supporting Information S1), particularly the longitude, and relative humidity (Figure S14 in Supporting Information S1) of the moisture source for the areas exhibiting positive temporal $\delta^{18}\text{O}_p$ -precipitation gradients. This suggests that changes in the isotopic composition of the source evaporative water vapor for those areas might contribute to the positive isotope-precipitation gradients. Nevertheless, only minor changes are found for the source SST (Figure S15 in Supporting Information S1) and surface wind (Figure S16 in Supporting Information S1). To evaluate the third possibility, we examine the differences in boreal summer $\delta^{18}\text{O}_p$ and

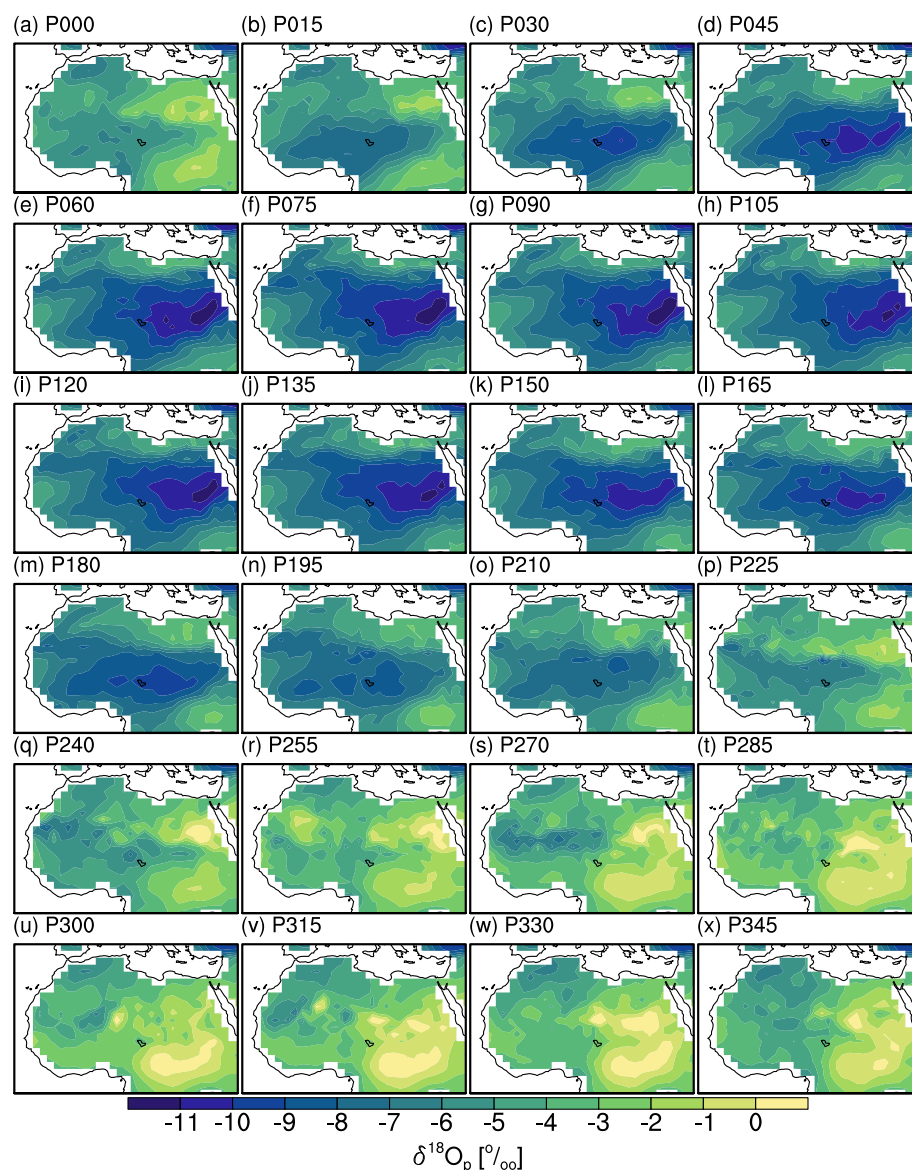


Figure 7. Precipitation-weighted annual mean $\delta^{18}O_p$ [‰].

precipitation patterns between two phases of the precession cycle. Our result, illustrated in Figures 10 and 11, indicates that the regions with positive isotope-precipitation gradients experience opposite precipitation changes in upstream areas, typically situated along western coastal oceans or continents. For example, in Figures 10c–10e, a strong reduction in precipitation is observed in the Gulf of Guinea and the nearby continental region, resulting in a more enriched heavier isotopic composition in the water vapor exported landward (Figures 11c–11e). Consequently, despite a local increase in rainfall quantity, the downstream inland areas experience higher values of $\delta^{18}O_p$, leading to a positive temporal $\delta^{18}O_p$ -precipitation gradient (Figures 9c–9e). Similarly, an increase in the intensity of precipitation rate near the western coast of Northern Africa as shown in Figures 10h–10j leads to more depleted $\delta^{18}O_p$ in the water vapor and in the subsequent precipitation in downstream inland areas (Figures 11h–11j), where a local decrease in precipitation is observed. This underlines the potential impact of upstream precipitation changes on the isotope composition of remaining water vapor and subsequent precipitation events. Thus, we propose that during the African humid periods, precipitation isotopic composition across the Northern African continent may reflect the degree of rainout occurring upstream. This finding underscores the general

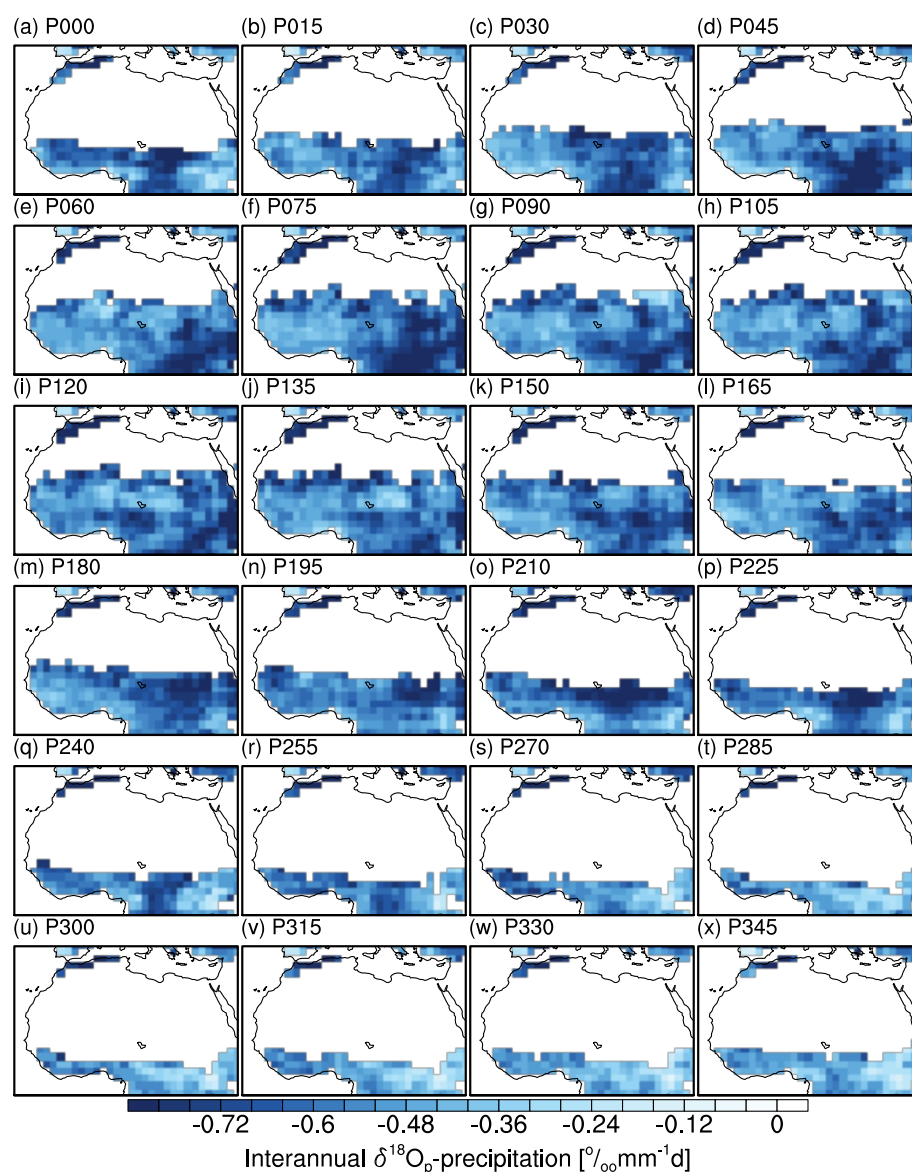


Figure 8. Interannual gradients between monthly anomalies of oxygen-18 composition in precipitation ($\delta^{18}O_p$) and precipitation rate for each experiment. Units: $\text{‰mm}^{-1}\text{d}$.

necessity of considering precipitation changes along upstream water transport trajectories when interpreting isotope proxies of past climate changes.

4. Discussion and Conclusions

In the present study, we perform 24 time-slice experiments covering a full precession cycle, performed with the newly developed isotope-enabled climate model AWIESM2-wiso. Besides seasonal changes of climatic variables which have been explored in a number of previous studies (Bosmans et al., 2015; J. E. Kutzbach et al., 2020; Marzocchi et al., 2015; Tuenter et al., 2003, 2005), we focus our analyses on the responses of extreme events, lengths of summer monsoon on a regional scale, as well as $\delta^{18}O$ changes in precipitation to variations in precession.

To assess the validity of our model's isotope simulations, we compared the simulated summer δD anomalies between minimum and maximum precession phases with available proxy records from Northern Africa, specifically leaf wax δD data from site ODP 659 off the northwest African coast and the Chew Bahir region (R.

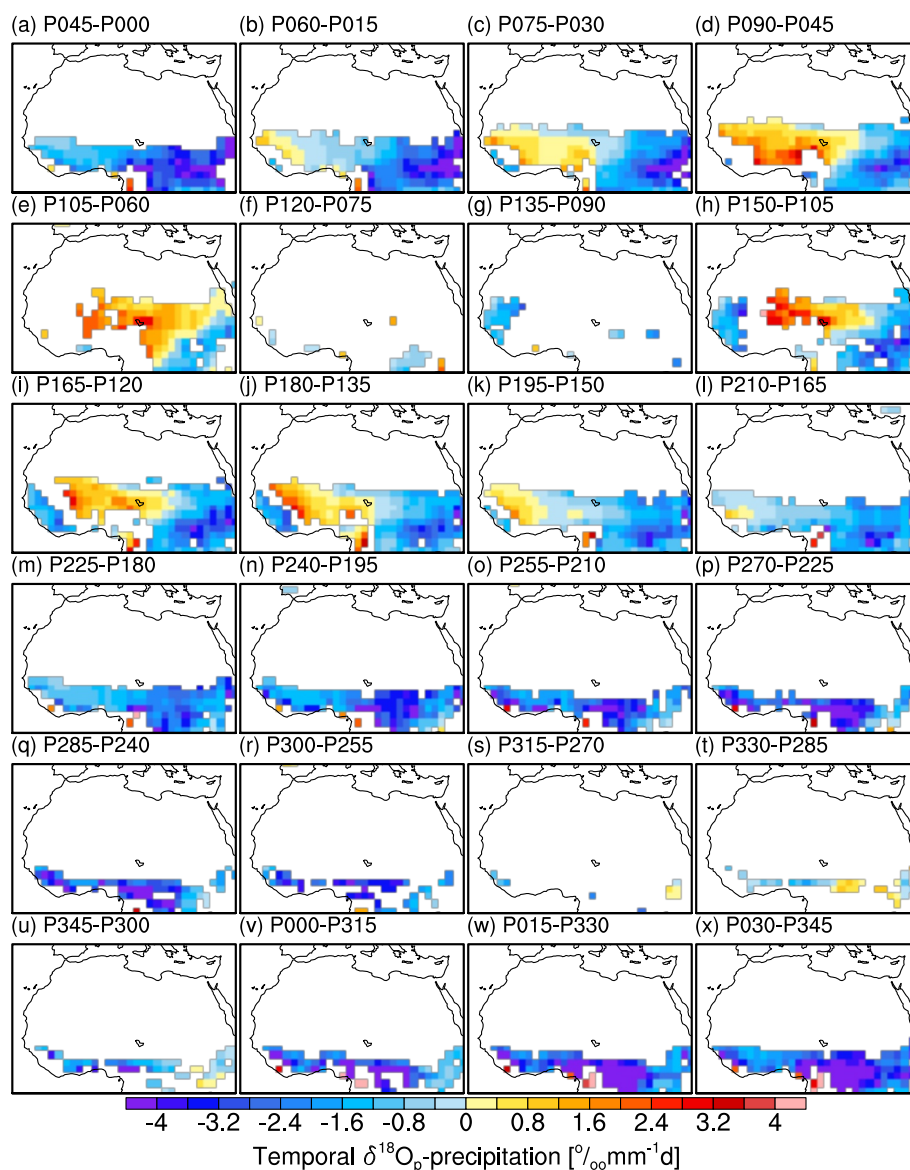


Figure 9. Simulated temporal $\delta^{18}\text{O}_p$ -precipitation gradients between two specific phases in a precession cycle. Units: $\text{‰mm}^{-1}\text{d}$.

Kuechler et al., 2013; Lupien et al., 2022). These records cover multiple precession cycles, spanning the period from 127 ka to present. Given that our experiments employ a high eccentricity, which more closely resembles conditions during the Eemian, we focused on comparing δD anomalies between 127 ka (minimum precession) and 116 ka (maximum precession). Our results show strong agreement with proxy data in both sign and magnitude, as illustrated in Figure S17 in Supporting Information S1. This model-data agreement strengthens confidence in our model's ability to reproduce isotope signals influenced by precession, supporting its utility in simulating paleoclimate conditions in Northern Africa.

Similar to Marzocchi et al. (2015) and Tuenter et al. (2003, 2005), in our model study, the spatio-temporal phasing of Northern Africa precipitation during JJAS shows a close relationship with solar radiation levels. Most regions experience the wettest summers between precession 105° and 120° , indicating spatial synchronization in the timing of maximum precipitation. In contrast, the timing of maximum surface air temperature (SAT_{max}) shows spatial heterogeneity and is influenced by different factors across Northern Africa: SAT_{max} in the northern part is paced by maximum insolation, while the tropical area experiences maximum cloud cover during phases with

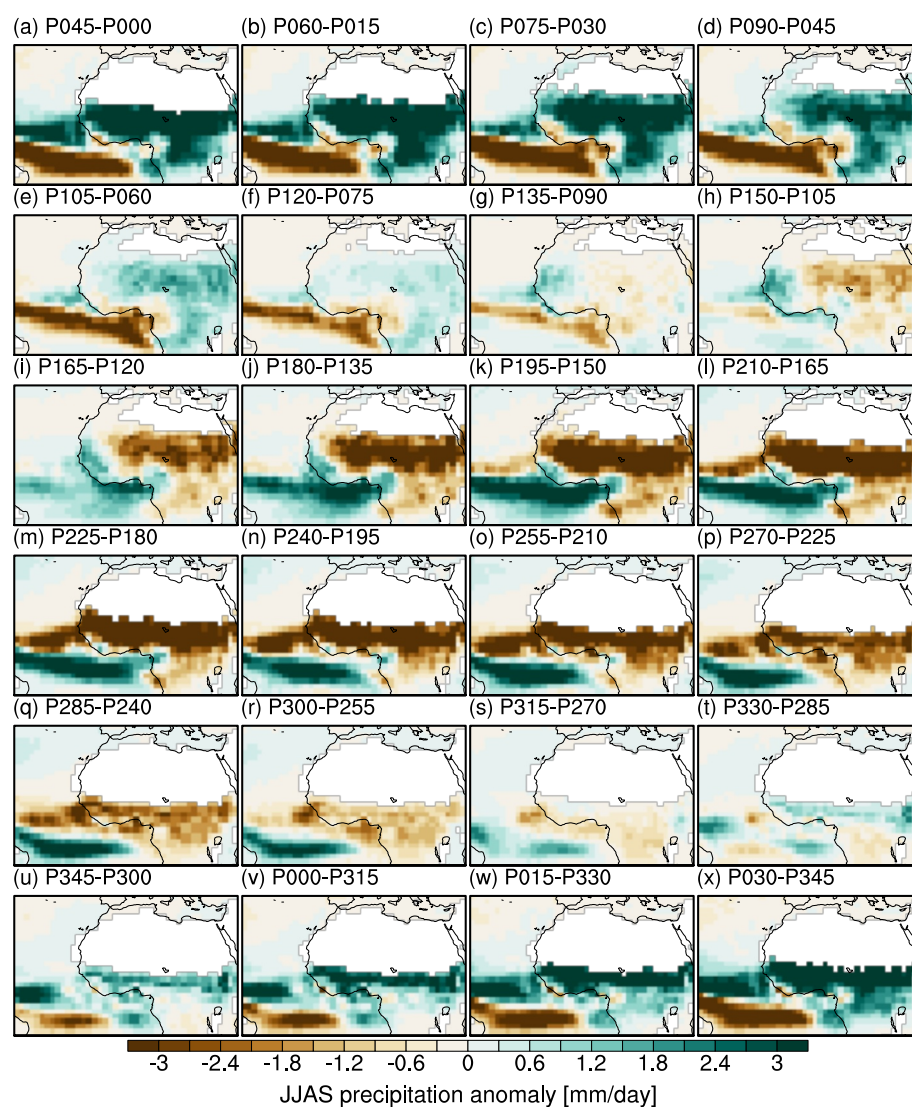


Figure 10. Simulated changes in JJAS precipitation between two specific phases in a precession cycle. Units: mm/day.

maximum convection, resulting in SAT_{max} being paced by minimum insolation. The phasing of SAT_{max} in the subtropical region is influenced by the intensities of both insolation and convection. This result is consistent with Marzocchi et al. (2015). On the other hand, the timing of minimum surface air temperature is more spatially synchronized, occurring around 90° precession across most areas of Northern Africa, closely following the timing of the minimum insolation.

This study also examines the variations in the onset and retreat of the West Africa Summer Monsoon (WASM) throughout a precession cycle. It is found that the typical onset of the WASM falls between early-June and mid-July, with advancements noted during precession phases of $0-105^\circ$ and delays observed in phases spanning $180-300^\circ$. The phasing of WASM onset is paced by the intensity of the Sahara Heat Low (SHL) in June and $0-25^\circ N$ insolation magnitude in May. Earlier (later) retreat of the WASM occurs during precession phases of $345-30^\circ$ ($225-300^\circ$), prominently influenced by insolation during August-September and the latitudinal displacement of peak insolation. The duration of the WASM is largely shaped by the timing of withdrawal across a precession cycle. Our result is in agreement with most PMIP4 models that reveal a shorter duration of WASM during the Last interglacial (with a precession of 95.4°) compared to pre-industrial (with a precession of 280.3°) (Shi et al., 2024). Our study shows that the difference in WASM duration between difference precession phases can reach 70 days. Our results shed light on the hydroclimatic conditions that may have contributed to the “Green Sahara” phases. A

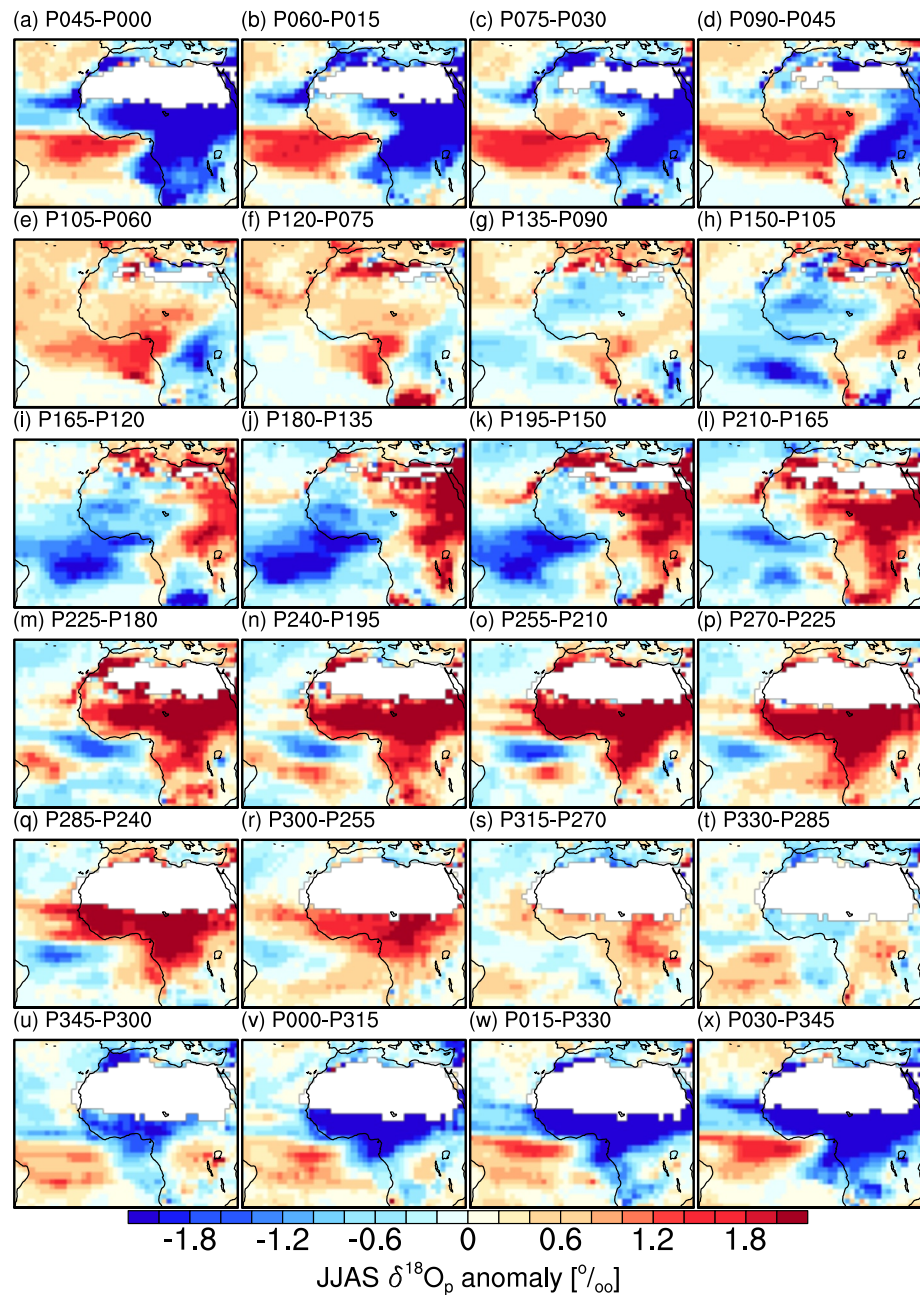


Figure 11. Simulated changes in JJAS $\delta^{18}\text{O}_p$ between two specific phases in a precession cycle. Units: ‰.

key question in understanding these intervals has been whether the enhanced vegetation cover is primarily due to increased precipitation rate, an extended rainy season, or both. Our experiments reveal that during these Green Sahara periods, the rainy season itself is relatively short, suggesting that the vegetation expansion was largely driven by an increase in precipitation rate rather than a prolonged monsoon duration. This implies that a more intense, though seasonally restricted, rainfall would have still provided sufficient moisture to sustain expanded vegetation and create conditions conducive to prolonged soil moisture.

Our model results regarding changes in CDD and CWD provide insight into how extreme dry and wet spells might shape vegetation and length of the growing season in a precession cycle. In environments with frequent and prolonged dry spells (e.g., P270), soil moisture gradually diminishes, making it challenging for vegetation that requires a high amount of water to survive (Nepstad et al., 2002; Vicente-Serrano et al., 2013). In such conditions,

drought-resistant vegetation types, such as shrubs, grasses, or certain drought-tolerant trees, tend to dominate (Chesson et al., 2004). In contrast, when wet spells are prolonged (e.g., P090), soil moisture remains high, supporting the growth of deep-rooted vegetation types such as forests. The variation in these wet and dry spells also impacts the length of the growing season (Zhang et al., 2018). Stable water availability supports longer growing seasons, while frequent CDDs force vegetation to adapt to seasonal water shortages.

An innovative scale-flux tracing method (Gao et al., 2024) is applied in our simulations to quantify the spatial and temporal changes in moisture source regions and properties throughout a precession cycle. Rainfall in western Africa mostly stems from the Atlantic Ocean, while in eastern Africa it predominantly stems from the Indian Ocean. During the transition from minimum to maximum precession, there is a rise (reduction) in the proportion of Northern Africa's precipitation sourced from the Indian (Atlantic) Ocean, and with a discernible increase in its susceptibility to the influence of evaporation from colder and less humid areas.

This study also investigates the isotopic composition of precipitation ($\delta^{18}\text{O}_p$) and its relationship with precipitation amounts across Northern Africa in different phases of a precession cycle. Negative interannual gradients between monthly $\delta^{18}\text{O}_p$ and precipitation rate align well with an explanation based on the classical “amount effect.” However, during precession phases characterized by a humid and lush Sahara, there is a distinct occurrence of a positive temporal $\delta^{18}\text{O}_p$ -precipitation gradient in specific areas of Northern Africa, which cannot be explained by an “amount effect.” For these regions, changes in locations and properties of moisture sources might influence the validity of the “amount effect.” More importantly, it is found that the changes in $\delta^{18}\text{O}_p$ in these areas are controlled by precipitation changes in upstream water vapor transport regions rather than changes in the amount of local rainfall, indicating that the interpretation of isotope signals documented in Northern African archives needs to be taken with caution. This finding is in good agreement to the proposed “upstream depletion” hypothesis suggested in previous studies on past isotope changes in the Asian monsoon region (Cheng et al., 2016; Hu et al., 2008; LeGrande & Schmidt, 2009; Z. Liu et al., 2014; Pausata et al., 2011; Tabor et al., 2018; Zhao et al., 2021). These studies suggest that the isotopic composition of (sub)tropical precipitation does not reflect local precipitation changes but rather the integrated changes in precipitation between tropical ocean source regions and a specific study region.

The results we obtained are based on idealized experimental setup to isolate the direct effects of precession on climate and water isotope signals in Northern Africa. While we acknowledge that the idealized setup limits the direct applicability of our results to real-world paleoclimate contexts, it provides a useful baseline for interpreting how precession alone may influence precipitation, temperature, and isotopes. More complex experimental designs that incorporate additional climate forcings such as greenhouse gases and ice sheets could further enhance our understanding of Northern African climate dynamics on orbital timescales.

Data Availability Statement

The model outputs related to the present study are available on Zenodo repository (Shi, 2024).

References

- Armstrong, E., Tallavaara, M., Hopcroft, P. O., & Valdes, P. J. (2023). North African humid periods over the past 800,000 years. *Nature Communications*, 14(1), 5549. <https://doi.org/10.1038/s41467-023-41219-4>
- Bartlein, P. J., & Shafer, S. L. (2019). Paleo calendar-effect adjustments in time-slice and transient climate-model simulations (paleocaladjust v1.0): Impact and strategies for data analysis. *Geoscientific Model Development*, 12(9), 3889–3913. <https://doi.org/10.5194/gmd-12-3889-2019>
- Berger, A., Yin, Q., & Wu, Z. (2024). Length of astronomical seasons, total and average insolation over seasons. *Quaternary Science Reviews*, 334, 108620. <https://doi.org/10.1016/j.quascirev.2024.108620>
- Bosmans, J., Drijfhout, S., Tuenter, E., Hilgen, F., & Lourens, L. (2015). Response of the North African summer monsoon to precession and obliquity forcings in the EC-earth GCM. *Climate Dynamics*, 44(1–2), 279–297. <https://doi.org/10.1007/s00382-014-2260-z>
- Brovkin, V., Boysen, L., Raddatz, T., Gayler, V., Loew, A., & Claussen, M. (2013). Evaluation of vegetation cover and land-surface albedo in MPI-ESM CMIP5 simulations. *Journal of Advances in Modeling Earth Systems*, 5(1), 48–57. <https://doi.org/10.1029/2012ms000169>
- Brovkin, V., Raddatz, T., Reick, C. H., Claussen, M., & Gayler, V. (2009). Global biogeophysical interactions between forest and climate. *Geophysical Research Letters*, 36(7), L07405. <https://doi.org/10.1029/2009gl037543>
- Cauquoin, A., & Werner, M. (2021). High-resolution nudged isotope modeling with ECHAM6-WISO: Impacts of updated model physics and ERA5 reanalysis data. *Journal of Advances in Modeling Earth Systems*, 13(11), e2021MS002532. <https://doi.org/10.1029/2021ms002532>
- Cauquoin, A., Werner, M., & Lohmann, G. (2019). Water isotopes—climate relationships for the mid-Holocene and preindustrial period simulated with an isotope-enabled version of MPI-ESM. *Climate of the Past*, 15(6), 1913–1937. <https://doi.org/10.5194/cp-15-1913-2019>
- Cheng, H., Edwards, R. L., Sinha, A., Spötl, C., Yi, L., Chen, S., et al. (2016). The Asian monsoon over the past 640,000 years and ice age terminations. *Nature*, 534(7609), 640–646. <https://doi.org/10.1038/nature18591>

Acknowledgments

The study is supported by the Southern Marine Science and Engineering Guangdong Laboratory (Zhuhai) (Grant SML2023SP204), the National Natural Science Foundation of China (NSFC) (Grant 42206256), the Ocean Negative Carbon Emissions (ONCE) Program, and the German Federal Ministry of Education and Science (BMBF) PalMod II WP 3.3 (Grant 01LP1924B). QG has received funding from the European Union's Horizon 2020 research and innovation programme under the Marie Skłodowska-Curie (Grant 955750). The simulations were conducted on Deutsche Klimarechenzentrum (DKRZ).

- Cheng, H., Zhang, P., Spötl, C., Edwards, R., Cai, Y., Zhang, D., et al. (2012). The climatic cyclicity in semiarid central Asia over the past 500,000 years. *Geophysical Research Letters*, *39*(1), L01705. <https://doi.org/10.1029/2011gl015020>
- Chesson, P., Gebauer, R. L., Schwinning, S., Huntly, N., Wiegand, K., Ernest, M. S., et al. (2004). Resource pulses, species interactions, and diversity maintenance in arid and semi-arid environments. *Oecologia*, *141*(2), 236–253. <https://doi.org/10.1007/s00442-004-1551-1>
- Danilov, S., Sidorenko, D., Wang, Q., & Jung, T. (2017). The finite-volume sea ice–ocean model (fesom2). *Geoscientific Model Development*, *10*(2), 765–789. <https://doi.org/10.5194/gmd-10-765-2017>
- Dansgaard, W. (1964). Stable isotopes in precipitation. *Tellus*, *16*(4), 436–468. <https://doi.org/10.1111/j.2153-3490.1964.tb00181.x>
- Fiorella, R. P., Siler, N., Nusbaumer, J., & Noone, D. C. (2021). Enhancing understanding of the hydrological cycle via pairing of process-oriented and isotope ratio tracers. *Journal of Advances in Modeling Earth Systems*, *13*(10), e2021MS002648. <https://doi.org/10.1029/2021ms002648>
- Fleitmann, D., Burns, S. J., Neff, U., Mudelsee, M., Mangini, A., & Matter, A. (2004). Palaeoclimatic interpretation of high-resolution oxygen isotope profiles derived from annually laminated speleothems from southern Oman. *Quaternary Science Reviews*, *23*(7–8), 935–945. <https://doi.org/10.1016/j.quascirev.2003.06.019>
- Gao, Q., Sime, L. C., McLaren, A. J., Bracegirdle, T. J., Capron, E., Rhodes, R. H., et al. (2024). Evaporative controls on Antarctic precipitation: An ECHAM6 model study using innovative water tracer diagnostics. *The Cryosphere*, *18*(2), 683–703. <https://doi.org/10.5194/tc-18-683-2024>
- Gimeno, L., Nieto, R., & Sorì, R. (2020). The growing importance of oceanic moisture sources for continental precipitation. *Npj Climate and Atmospheric Science*, *3*(1), 27. <https://doi.org/10.1038/s41612-020-00133-y>
- Gong, C., & Eltahir, E. (1996). Sources of moisture for rainfall in West Africa. *Water Resources Research*, *32*(10), 3115–3121. <https://doi.org/10.1029/96wr01940>
- Haese, B., Werner, M., & Lohmann, G. (2013). Stable water isotopes in the coupled atmosphere–land surface model ECHAM5-JSBACH. *Geoscientific Model Development*, *6*(5), 1463–1480. <https://doi.org/10.5194/gmd-6-1463-2013>
- Hu, C., Henderson, G. M., Huang, J., Xie, S., Sun, Y., & Johnson, K. R. (2008). Quantification of Holocene Asian monsoon rainfall from spatially separated cave records. *Earth and Planetary Science Letters*, *266*(3–4), 221–232. <https://doi.org/10.1016/j.epsl.2007.10.015>
- Jiang, Z., Jiang, S., Shi, Y., Liu, Z., Li, W., & Li, L. (2017). Impact of moisture source variation on decadal-scale changes of precipitation in north China from 1951 to 2010. *Journal of Geophysical Research: Atmospheres*, *122*(2), 600–613. <https://doi.org/10.1002/2016jd025795>
- Johnson, K. R., Ingram, B. L., Sharp, W. D., & Zhang, P. (2006). East Asian summer monsoon variability during marine isotope stage 5 based on speleothem $\delta^{18}\text{O}$ records from Wanxiang Cave, central China. *Paleogeography, Palaeoclimatology, Palaeoecology*, *236*(1–2), 5–19. <https://doi.org/10.1016/j.palaeo.2005.11.041>
- Joussaume, S., & Braconnot, P. (1997). Sensitivity of paleoclimate simulation results to season definitions. *Journal of Geophysical Research*, *102*(D2), 1943–1956. <https://doi.org/10.1029/96jd01989>
- Ku, T., & Li, H. (1998). Speleothems as high-resolution paleoenvironment archives: Records from northeastern China. *Journal of Earth System Science*, *107*(4), 321–330. <https://doi.org/10.1007/bf02841598>
- Kuechler, R., Schefuß, E., Beckmann, B., Dupont, L., & Wefer, G. (2013). Nw African hydrology and vegetation during the last glacial cycle reflected in plant-wax-specific hydrogen and carbon isotopes. *Quaternary Science Reviews*, *82*, 56–67. <https://doi.org/10.1016/j.quascirev.2013.10.013>
- Kuechler, R. R., Dupont, L. M., & Schefuß, E. (2018). Hybrid insolation forcing of Pliocene monsoon dynamics in West Africa. *Climate of the Past*, *14*(1), 73–84. <https://doi.org/10.5194/cp-14-73-2018>
- Kutzbach, J., Chen, G., Cheng, H., Edwards, R., & Liu, Z. (2014). Potential role of winter rainfall in explaining increased moisture in the Mediterranean and middle east during periods of maximum orbitally-forced insolation seasonality. *Climate Dynamics*, *42*(3–4), 1079–1095. <https://doi.org/10.1007/s00382-013-1692-1>
- Kutzbach, J. E., Guan, J., He, F., Cohen, A. S., Orland, I. J., & Chen, G. (2020). African climate response to orbital and glacial forcing in 140,000-y simulation with implications for early modern human environments. *Proceedings of the National Academy of Sciences*, *117*(5), 2255–2264. <https://doi.org/10.1073/pnas.1917673117>
- Lachniet, M. S. (2009). Climatic and environmental controls on speleothem oxygen-isotope values. *Quaternary Science Reviews*, *28*(5–6), 412–432. <https://doi.org/10.1016/j.quascirev.2008.10.021>
- Larrasoana, J., Roberts, A., Rohling, E., Winkhofer, M., & Wehausen, R. (2003). Three million years of monsoon variability over the northern Sahara. *Climate Dynamics*, *21*(7–8), 689–698. <https://doi.org/10.1007/s00382-003-0355-z>
- LeGrande, A., & Schmidt, G. (2009). Sources of Holocene variability of oxygen isotopes in paleoclimate archives. *Climate of the Past*, *5*(3), 441–455. <https://doi.org/10.5194/cp-5-441-2009>
- Levitus, S., Locarnini, R. A., Boyer, T. P., Mishonov, A. V., Antonov, J. I., Garcia, H. E., et al. (2010). World ocean atlas 2009.
- Liu, X., Liu, J., Chen, S., Chen, J., Zhang, X., Yan, J., & Chen, F. (2020). New insights on Chinese cave $\delta^{18}\text{O}$ records and their paleoclimatic significance. *Earth-Science Reviews*, *207*, 103216. <https://doi.org/10.1016/j.earscirev.2020.103216>
- Liu, Z., Wen, X., Brady, E., Otto-Bliesner, B., Yu, G., Lu, H., et al. (2014). Chinese cave records and the East Asia summer monsoon. *Quaternary Science Reviews*, *83*, 115–128. <https://doi.org/10.1016/j.quascirev.2013.10.021>
- Lourens, L. J., Wehausen, R., & Brumsack, H. J. (2001). Geological constraints on tidal dissipation and dynamical ellipticity of the earth over the past three million years. *Nature*, *409*(6823), 1029–1033. <https://doi.org/10.1038/35059062>
- Lupien, R. L., Russell, J. M., Pearson, E. J., Castañeda, I. S., Asrat, A., Foerster, V., et al. (2022). Orbital controls on eastern African hydroclimate in the pleistocene. *Scientific Reports*, *12*(1), 3170. <https://doi.org/10.1038/s41598-022-06826-z>
- Maher, B. A. (2008). Holocene variability of the East Asian summer monsoon from Chinese cave records: A re-assessment. *The Holocene*, *18*(6), 861–866. <https://doi.org/10.1177/0959683608095569>
- Marzocchi, A., Lunt, D. J., Flecker, R., Bradshaw, C. D., Farnsworth, A., & Hilgen, F. J. (2015). Orbital control on late Miocene climate and the North African monsoon: Insight from an ensemble of sub-precessional simulations. *Climate of the Past*, *11*(10), 1271–1295. <https://doi.org/10.5194/cp-11-1271-2015>
- McManus, J. F., Oppo, D. W., & Cullen, J. L. (1999). A 0.5-million-year record of millennial-scale climate variability in the north Atlantic. *Science*, *283*(5404), 971–975. <https://doi.org/10.1126/science.283.5404.971>
- Nepstad, D., Moutinho, P., Dias-Filho, M., Davidson, E., Cardinot, G., Markewitz, D., et al. (2002). The effects of partial throughfall exclusion on canopy processes, aboveground production, and biogeochemistry of an amazon forest. *Journal of Geophysical Research*, *107*(D20), LBA–53. <https://doi.org/10.1029/2001jd000360>
- Odoulami, R. C., & Akinsanola, A. (2018). Recent assessment of west African summer monsoon daily rainfall trends. *Weather*, *73*(9), 283–287. <https://doi.org/10.1002/wea.2965>
- Orland, I. J., Edwards, R. L., Cheng, H., Kozdon, R., Cross, M., & Valley, J. W. (2015). Direct measurements of deglacial monsoon strength in a Chinese stalagmite. *Geology*, *43*(6), 555–558. <https://doi.org/10.1130/g36612.1>

- Otto-Bliesner, B., Braconnot, P., Harrison, S., Lunt, D., Abe-Ouchi, A., Albani, S., et al. (2017). The PMIP4 contribution to CMIP6—part 2: Two interglacials, scientific objective and experimental design for Holocene and last interglacial simulations. *Geoscientific Model Development*, 10(11), 3979–4003. <https://doi.org/10.5194/gmd-10-3979-2017>
- Pausata, F. S., Battisti, D. S., Nisancioglu, K. H., & Bitz, C. M. (2011). Chinese stalagmite $\delta^{18}\text{O}$ controlled by changes in the Indian monsoon during a simulated Heinrich event. *Nature Geoscience*, 4(7), 474–480. <https://doi.org/10.1038/ngeo1169>
- Pausata, F. S., Messori, G., & Zhang, Q. (2016). Impacts of dust reduction on the northward expansion of the African monsoon during the green Sahara period. *Earth and Planetary Science Letters*, 434, 298–307. <https://doi.org/10.1016/j.epsl.2015.11.049>
- Pokras, E. M., & Mix, A. C. (1987). Earth's precession cycle and quaternary climatic change in tropical Africa. *Nature*, 326(6112), 486–487. <https://doi.org/10.1038/326486a0>
- Raddatz, T., Reick, C., Knorr, W., Kattge, J., Roeckner, E., Schnur, R., et al. (2007). Will the tropical land biosphere dominate the climate–carbon cycle feedback during the twenty-first century? *Climate Dynamics*, 29(6), 565–574. <https://doi.org/10.1007/s00382-007-0247-8>
- Reick, C., Raddatz, T., Brovkin, V., & Gayler, V. (2013). Representation of natural and anthropogenic land cover change in MPI-ESM. *Journal of Advances in Modeling Earth Systems*, 5(3), 459–482. <https://doi.org/10.1002/jame.20022>
- Reick, C. H., Gayler, V., Goll, D., Hagemann, S., Heidkamp, M., Nabel, J. E., et al. (2021). JSBACH 3—the land component of the MPI earth system model: Documentation of version 3.2.
- Risi, C., Bony, S., Vimeux, F., & Jouzel, J. (2010). Water-stable isotopes in the LMDZ4 general circulation model: Model evaluation for present-day and past climates and applications to climatic interpretations of tropical isotopic records. *Journal of Geophysical Research*, 115(D12), D12118. <https://doi.org/10.1029/2009jd013255>
- Roche, D. M., & Caley, T. (2013). $\delta^{18}\text{O}$ water isotope in the iLOVECLIM model (version 1.0)—part 2: Evaluation of model results against observed $\delta^{18}\text{O}$ in water samples. *Geoscientific Model Development*, 6(5), 1493–1504. <https://doi.org/10.5194/gmd-6-1493-2013>
- Roeckner, E., Brokopf, R., Esch, M., Giorgetta, M., Hagemann, S., Kornbluh, L., et al. (2004). The atmospheric general circulation model echem5 part ii: Sensitivity of simulated climate to horizontal and vertical resolution.
- Rosignol-Strick, M. (1985). Mediterranean quaternary sapropels, an immediate response of the african monsoon to variation of insolation. *Palaeogeography, Palaeoclimatology, Palaeoecology*, 49(3–4), 237–263. [https://doi.org/10.1016/0031-0182\(85\)90056-2](https://doi.org/10.1016/0031-0182(85)90056-2)
- Schmidt, G. A., LeGrande, A. N., & Hoffmann, G. (2007). Water isotope expressions of intrinsic and forced variability in a coupled ocean-atmosphere model. *Journal of Geophysical Research*, 112(D10), D10103. <https://doi.org/10.1029/2006jd007781>
- Shi, X. (2024). Precession experiments based on awiesm2-wiso [Dataset]. *zenodo*. <https://doi.org/10.5281/zenodo.13314067>
- Shi, X., Cauquoin, A., Lohmann, G., Jonkers, L., Wang, Q., Yang, H., et al. (2023). Simulated stable water isotopes during the mid-Holocene and pre-industrial periods using AWI-ESM-2.1-WISO. *Geoscientific Model Development*, 16(17), 5153–5178. <https://doi.org/10.5194/gmd-16-5153-2023>
- Shi, X., Werner, M., Krug, C., Brierley, C. M., Zhao, A., Igbino, E., et al. (2022). Calendar effects on surface air temperature and precipitation based on model-ensemble equilibrium and transient simulations from PMIP4 and PACMEDY. *Climate of the Past*, 18(5), 1047–1070. <https://doi.org/10.5194/cp-18-1047-2022>
- Shi, X., Werner, M., Pausata, F. S., Yang, H., Liu, J., D'Agostino, R., et al. (2024). On the length and intensity of the West African summer monsoon during the last interglacial African humid period. *Quaternary Science Reviews*, 328, 108542. <https://doi.org/10.1016/j.quascirev.2024.108542>
- Stevens, B., Giorgetta, M., Esch, M., Mauritsen, T., Crueger, T., Rast, S., et al. (2013). Atmospheric component of the MPI-m earth system model: ECHAM6. *Journal of Advances in Modeling Earth Systems*, 5(2), 146–172. <https://doi.org/10.1002/jame.20015>
- Sultan, B., & Janicot, S. (2003). The West African monsoon dynamics. Part II: The “preonset” and “onset” of the summer monsoon. *Journal of Climate*, 16(21), 3407–3427. [https://doi.org/10.1175/1520-0442\(2003\)016<3407:twamdp>2.0.co;2](https://doi.org/10.1175/1520-0442(2003)016<3407:twamdp>2.0.co;2)
- Tabor, C. R., Otto-Bliesner, B. L., Brady, E. C., Nusbaumer, J., Zhu, J., Erb, M. P., et al. (2018). Interpreting precession-driven $\delta^{18}\text{O}$ variability in the south Asian monsoon region. *Journal of Geophysical Research: Atmospheres*, 123(11), 5927–5946. <https://doi.org/10.1029/2018jd028424>
- Tan, L., Li, Y., Wang, X., Cai, Y., Lin, F., Cheng, H., et al. (2020). Holocene monsoon change and abrupt events on the western Chinese loess plateau as revealed by accurately dated stalagmites. *Geophysical Research Letters*, 47(21), e2020GL090273. <https://doi.org/10.1029/2020gl090273>
- Tuenter, E., Weber, S., Hilgen, F., & Lourens, L. (2003). The response of the African summer monsoon to remote and local forcing due to precession and obliquity. *Global and Planetary Change*, 36(4), 219–235. [https://doi.org/10.1016/s0921-8181\(02\)00196-0](https://doi.org/10.1016/s0921-8181(02)00196-0)
- Tuenter, E., Weber, S., Hilgen, F., Lourens, L., & Ganopolski, A. (2005). Simulation of climate phase lags in response to precession and obliquity forcing and the role of vegetation. *Climate Dynamics*, 24(2–3), 279–295. <https://doi.org/10.1007/s00382-004-0490-1>
- Van der Laan, E., Hilgen, F., Lourens, L., De Kaenel, E., Gaboardi, S., & Iaccarino, S. (2012). Astronomical forcing of northwest African climate and glacial history during the late Messinian (6.5–5.5 ma). *Palaeogeography, Palaeoclimatology, Palaeoecology*, 313, 107–126. <https://doi.org/10.1016/j.palaeo.2011.10.013>
- Vicente-Serrano, S. M., Gouveia, C., Camarero, J. J., Beguería, S., Trigo, R., López-Moreno, J. I., et al. (2013). Response of vegetation to drought time-scales across global land biomes. *Proceedings of the National Academy of Sciences*, 110(1), 52–57. <https://doi.org/10.1073/pnas.1207068110>
- Zhang, W., Brandt, M., Tong, X., Tian, Q., & Fensholt, R. (2018). Impacts of the seasonal distribution of rainfall on vegetation productivity across the Sahel. *Biogeosciences*, 15(1), 319–330. <https://doi.org/10.5194/bg-15-319-2018>
- Zhao, C., Cheng, J., Wang, J., Yan, H., Leng, C., Zhang, C., et al. (2021). Paleoclimatic significance of reconstructed rainfall isotope changes in Asian monsoon region. *Geophysical Research Letters*, 48(12), e2021GL092460. <https://doi.org/10.1029/2021gl092460>